Diamond detectors for hadron physics research

E. Berdermann [a,*], M. Pomorski [a], W. de Boer [b], M. Ciobanu [a], S. Dunst [c], C. Grah [d], M. Kiš [a], W. Koenig [a], W. Lange [d], W. Lohmann [d], R. Lovrinčić [e], P. Moritz [a], J. Morse [f], S. Mueller [b], A. Pucci [e], M. Schreck [c], S. Rahman [a], M. Träger [a]

[a] GSI, Helmholtz Zentrum für Schwerionenforschung, Darmstadt, Germany
[b] Universität Karlsruhe, Germany
[c] Universität Augsburg, Germany
[d] DESY-Zeuthen, Berlin, Germany
[e] Ruprecht-Karls Universität Heidelberg, Germany
[f] European Synchrotron Radiation Facility, Grenoble, France

ARTICLE INFO

ABSTRACT

The application of diamond for the detection of charged particles in atomic, nuclear and high-energy physics experiments is described. We compare the properties of three undoped diamond types, all of them produced by Chemical Vapor Deposition (CVD), in particular homoepitaxial single-crystal CVD Diamond (scCVDD), polycrystalline CVD Diamond (pcCVDD) grown on silicon, and CVD Diamond on Iridium (DoI) grown on the multi-layer substrate Ir/YSZ/Si001. The characteristics of the transient current (TC) signals generated from ^{241}Am-α-particles in the samples are exploited to evaluate the potential of the diamond crystals for particle timing and spectroscopy applications. The TC technique (TCT) results are correlated to the dark conductivity and the structural defects of the bulk materials as well as to the morphology and roughness of the diamond surfaces. The deterioration of the sensors performance after heavy irradiations with 26 MeV protons, 20 MeV neutrons, and 10 MeV electrons is discussed by means of charge-collection efficiency results, TC technique, and optical absorption spectroscopy (OAS). The important role of the diamond signal processing is underlined, which influences both the quality of the CVDD characterization data as well as the in-beam performance of the diamond sensors.

© 2009 Elsevier B.V. All rights reserved.

1. Introduction

The term hadron physics will henceforth denote the basic research which comprises atomic, nuclear, and high-energy physics experiments. The fundamental interactions and forces, which define the structure of matter from quarks to galaxies, are studied using complementary probes, for instance, charged particles from protons to uranium, electrons, neutrons, X and γ-rays. Over more than one decade, CVD-diamond sensors have been investigated for applications in these related research fields [1–5]. The radiation resistance of diamond [1,6] was initially the most interesting property; it was assumed that it is higher than the one of any other comparable detector material. However, the scientific communities are still somehow hesitant to approve diamonds on a large scale. The higher costs as compared for instance to novel 'radiation hard' silicon devices [7], has to be compensated by additional advantages and by the superior characteristics of the diamond detectors.

In this review we discuss the sensor categories in which electronic grade pcCVDD and scCVDD have currently the potential to compete with traditional sensors (Section 2). We present first results obtained from a DoI CVDD plate [8] prepared at the University of Augsburg, which belongs to a CVDD type promising to combine the timing properties of pcCVDD [2] with an improved crystal homogeneity. Section 3 is dedicated to the signal processing; the sample preparation and the characterization of surface and bulk structure are described in Sections 4.1 and 4.2, the behavior of the dark conductivity in Section 4.3, and the TCT results throughout obtained using ^{241}Am-α-particles in Section 4.4. The performance of scCVDD sensors after intense proton, neutron, and electron irradiations is discussed in Section 4.6. The results are eventually summarized and concluded in Section 5.

2. Charged particle detection with diamond sensors

At 'hadron' accelerator facilities, the structure of matter is investigated performing collision experiments in the energy range of $1\,\mathrm{AMeV} \leq E_{beam} \leq 1\,\mathrm{ATeV}$ of ions ranging from protons to uranium. The colliding particles (henceforth denominated projectile and target ions) decay after interaction into a number of reaction products defined by the energy dissipated in the colliding system; the amount of the charged products in one event varies from 2 up to more than 1000. At the highest dissipated energy the colliding ions disintegrate into their constituent

quarks and their bonding particles, the gluons, forming a new state of matter called 'quark–gluon plasma' [9] which is believed to describe the structure of the universe shortly after the Big Bang.

The investigation of new rare processes requires unprecedented high beam intensities (up to $\sim 10^{12}$/beam pulse). At the upcoming Facility for Antiprotons and Ion Research (FAIR) in Darmstadt as well as at the Large Hadron Collider LHC and its upgrade SuperLHC at CERN or at the upcoming International Linear Collider (ILC), the detector systems located in the vicinity of the beam interaction zones have to withstand integral rates of $\geq 10^{16}$ particles/cm^2. In fixed-target experiments at GSI Darmstadt (Helmholtz Center for Heavy Ion Research), radiation hard, ultra-fast *start detectors* of low material budget are applied to start time-of-flight (ToF) measurements in order to define the time-zero (T0) of the beam-target interactions of interest out of total collision rates which are eight orders of magnitude higher than the physics process which is investigated. The potential of pcCVDD as well as of scCVDD in such *ion-ToF applications* is superior to any other known detector material. The same is valid for *single-particle beam and beam-loss monitoring* at ion rates far beyond 10^8 particles/s [10] as well as the *conditioning of ultra-relativistic beams* of minimum-ionizing particles (MIP) [11] and *beamstrahlung calorimetry* at high luminosity linear colliders [12].

Energy or energy-loss measurement techniques are powerful tools for *particle identification* (PID) in nuclear physics experiments. Each detector signal corresponds to the specific energy$-dE/dx$ dissipated per unit path length from an impinging ion in its bulk material; the 'stopping power'$-dE/dx$ of each target/sensor material is characteristic for the nuclear charge Z and the velocity β of the impinging ion and can be calculated according Ref. [13]. The generated charge Q_G increases with the ratio Z_{eff}^2/β^2 (with Z_{eff} the atomic charge state of the ion) and with the density of the detector material; it does not depend directly on the energy E or the mass m_{ion} of the ion. It should be noticed for the following that, since ions have the same velocity when they have the same value of E/m_{ion}, the hybrid unit E/A with $A = m_{ion}$ reflects β. A is the atomic mass number of the ion in units of 1/12 of the mass of ^{12}C.

At high relativistic velocities, all ions are usually fully ionized ($Z_{eff} \rightarrow Z$) and the energy-loss of the ions differs by Z^2. High-resolution MUltiple Sampling Ionization Chambers (MUSICs) are implemented to cover the large solid angles of the reactions, whereas in low-energy measurements $\Delta E - E$ silicon telescopes are used. However, if small-area devices are acceptable, scCVDD detectors are a serious alternative to classical sensors [14]. Note that this PID method do not apply for ultra-relativistic physics experiments, where all particles involved are minimum-ionizing and of $Z = 1$. The energy-loss signals of those are almost equal and therefore indistinguishable for a single sensor.

The ion mass is defined by particle tracking in magnetic fields combined with velocity measurements either by ion-ToF for moderate particle velocities, or by RICH (ring-imaging Čerencov hodoscopes) techniques in the relativistic ion case. For heavy-ion *tracking and ToF* systems at FAIR pcCVDD sensors are a reasonable alternative to silicon detectors [15]. However, the requirements of vertex devices (MIP detection) are hardly met by this type of diamond. In contrast to CERN experiments, the sensor thickness of at least 300 to 500 μm needed is not acceptable in measurements performed at projectile energies of $E_{max} \sim 30 AGeV$ (ions) or $E_{max} \sim 90$ GeV (protons and antiprotons). Monolithic pixel devices of a total material budget of only 200 μm silicon are projected for the Compressed Baryonic Matter (CBM) experiment, in order to minimize energy straggling and secondary reactions. Even worse is the application of pcCVDD for *start detectors of relativistic proton measurements*, which is an urgently needed detector type for both the present GSI and the future FAIR experiments. Spectroscopic grade scCVDD of extremely high breakdown field is required (Section 4.1) in addition to optimized broadband assemblies of improved signal-to-noise (S/N) ratio (Section 3).

3. Diamond signal processing

We refer henceforth to a 'diamond detector' assuming an (100)-oriented intrinsic diamond crystal of thickness, d_D, metallized with sandwich electrodes (the sensor) and connected to an amplifier. In the equilibrium state, the sensor is biased with $V_b = d_D \cdot E_D$, where E_D is a positive or negative electric field applied in the (100) direction of the crystal. The simplified equivalent schematics of the two alternative readout schemes are shown in Fig. 1: the low-impedance broadband (BB) signal processing applied for time measurements and the high-impedance charge-sensitive (CS) readout of limited bandwidth used for charge measurements.

The left hand part of this schematics belongs to both circuits consisting of the diamond sensor (framed) described by its capacitance C_D and a current generator, the bias circuit represented by V_b and a bias resistor, R_b, as well as various electronic components depicted by the thermal noise current generator $i_{nRi,f}$. The inherent noise of diamond sensors is negligible (intrinsic carrier density $N_i^{Dia} \approx 10^{-27}$/cm^3), and (for simplicity) we neglected also the parasitic capacitances C_p, which otherwise play a crucial role for the detector performance. In the right hand part of the figure are depicted a timing amplifier (i.e., a current amplifier) represented by its input impedance R_i and a coupling capacitance C_c (solid lines scheme) as well as, alternatively, a spectroscopy preamplifier (dashed lines scheme) represented by its feedback circuit $C_f \Leftrightarrow R_f$. A detailed description of the diamond signal creation, propagation, and processing can be found in [16].

For heavy-ion timing and TCT with ^{241}Am-α-sources in the laboratory, we developed a diamond broadband amplifier (DBA [17]), which is an inverting, AC coupled current amplifier of a bandwidth BW from 1 MHz to 2.3 GHz, an $R_i = 50 \Omega$, input capacitance $C_i = 5$ pF, and a low bias resistor $R_b = 10$ kΩ enabling high rate operation. Energy and energy-loss measurements are performed with CSTA2 spectroscopy preamplifiers originally developed for heavy-ion silicon sensors at the Technical University of Darmstadt. For the alpha measurements, the CSTA2 parameters are modified to $C_f = 1$ pF, $R_f = 1$ GΩ, $R_b = 1$ GΩ. The preamplifier signals are amplified and shaped by commercial shaping amplifiers (Canberra or ORTEC) and digitized with 13bit peak-sensing SILENA ADCs.

In an ideal detector, the particle induced transient current $I_{tr}(t)$ is described by the simplified Eq. (1)

$$I_{tr}(t,E) = \frac{Q_G \cdot v(E)}{d_D} \cdot e^{-(t/\tau)-(t/RC)} = \frac{Q_C(E)}{t_{tr}} \cdot e^{-t/R_iC} \qquad (1)$$

where Q_G and $Q_C(E)$ are the ion-generated and the collected charge at field E, respectively, d_D is the detector thickness, $v(E)$ the carrier
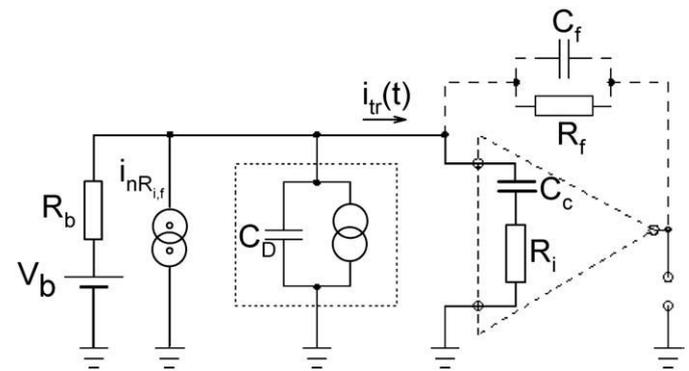
Fig. 1. Simplified equivalent schematics of a diamond sensor (framed) connected to the two kinds of preamplifiers used alternatively for hadron physics detectors: A BB amplifier (short-dashed lines) represented by its input impedance R_i and a coupling capacitance C_c, as well as a CS preamplifier (long-dashed lines) represented by its feedback circuit Cf ⟺ Rf. The left hand part of the schematics, consisting of a bias circuit (V_b, R_b) and a noise current generator inRi which depicts the thermal noise of the electronic components, belongs to both circuits.

drift velocity, τ the lifetime of excess carriers, and R_iC the time constant of a circuit with $C = C_P + C_D$.

$I_{tr}(t, E)$ causes a fall and rise of V_b, resulting in case of BB processing in a voltage drop $U_{tr}(t,E) = \frac{U_0(E)}{R_i} \cdot e^{-t/R_iC}$ over the 50 Ω input impedance of the amplifier, which is recorded and analyzed with a LeCroy digital sampling oscilloscope (DSO) of 3 GHz bandwidth and 20 GS/s sampling rate. For minimized C_P and small C_D, the time constant of a BB setup is short (on the order of picoseconds), and the signal shape reflects the original charge drift and collection in the diamonds. The area of the BB signal is a measure for the collected charge: $Q_C(E) = \frac{1}{R_i}\int U_{tr}(t,E)dt$. In contrast, the time constant of the CS setup is on the order of a millisecond; the transient current is fully integrated at the feedback capacitance C_f, and the peak value of the output signal $U_{peak}(E) = \frac{\int I_{tr}(t,E)dt}{C_f} = \frac{Q_C(E)}{C_f}$ provides that way a more precise value for $Q_C(E)$ than the area of the BB signals—as it is required for particle identification.

Besides breakdown stability (Section 4.1), the ultimate detector quality parameters are the energy resolution ($\delta E/E$) defined by the widths of the collected charge distributions and the intrinsic time resolution σ_i, given by $\sigma_i = \sigma_{ToF}/\sqrt{2}$ with σ_{ToF}, the width of the ToF spectrum measured between two identical start-stop sensors located at a distance $d_{ToF} \sim 0$. Both resolutions depends on the S/N ratio, and the discriminator threshold is usually set as high as three times the standard deviation of the equivalent noise distribution N(rms) of the front-end electronics (FEE). In the following, we discuss the optimization of diamond detectors for time measurements of relativistic particles from protons to uranium ions.

The task is to develop sensors of lowest possible material budget (thickness) in order to limit secondary reactions. Whereas the collected charge Q_C corresponds to the area of the induced current signal (Eq. (1)), the crucial parameter for the design of timing electronics is the amplitude of the bias drop $|U_0|$ on R_i. According Eq. (1), it is not predicted a priori that scCVDD is always the best material choice. The calculation of the signal amplitudes of 'dual-carrier drift' mode signals in the 'space charge limited current' (SCLC) case is complicated [18] and needs correct simulation for precise results (not available at present). For the time being, we estimated roughly the pulse heights on the 50 Ω impedance of a DBA amplifier, which are expected from relativistic ions of 1 AGeV in CVDD sensors of different thicknesses 50 μm$<d_D<$400 μm and a charge-collection efficiency (CCE) in the range 0.1$<$CCE$<$0.6 for pcCVDD and CCE$\sim$1 for scCVDD, respectively. The results are plotted in Fig. 2.

The thick line indicates the equivalent DBA noise amplitude, $\sigma_{nDBA} \sim 50$ μV, and the dashed line above the $3\sigma_{nDBA}$ deviation noise amplitude. The transition times estimated for the SCCVDD case have been extrapolated from measured ^{131}Xe transients, which revealed a signal width of $\sim$2.5 ns on a 400 μm sensor [14]. For the widths of the pcCVDD sensors, a linear increase of the transition time with d_D has been considered [19], taken into account 100 ps for CCE = 0.1 and $\sim$1.5 ns for CCE = 0.6.

These data demonstrate impressively the large dynamic range of signals involved in hadron physics experiments. Furthermore, they show that the BB readout in the case of relativistic ions lighter than carbon (open circles) is challenging even with spectroscopic grade scCVDD sensors.

The dependence of the intrinsic time resolution σ_i on the TC signal shape parameters and on the electronic noise is described in Eq. (2)

$$\sigma_i = \frac{\sigma_{nDBA}}{dU(t)/dt} \tag{2}$$

with σ_{nDBA} the dispersion of the noise voltage, and dU/dt the leading edge slope of the signals at discriminator threshold [20,21].

We tested several assemblies equipped with quite different FEE (Table 1) developed at GSI. One approach was to use a fast integrating CS preamplifier (CSPA) at the front-end, followed by a broadband amplifier and discriminator card (FEE-1). Other designs have been: pure high-frequency readout with DBAs, a low-capacitance BB setup (LCBB) developed for the proton start detector of the HADES spectrometer [22], as well as a new wideband amplifier-discriminator ASIC named PADI-1 developed from the CBM and the FOPI Collaborations. The best heavy-ion result ($\sigma_i = 25$ ps) has been achieved with 'as grown' pcCVDD sensors of 100 μm thickness readout with FEE-1, whereas the highest resolution for relativistic protons ($\sigma_i = 100$ ps) has been obtained from scCVDD sensors of 400 μm thickness readout with LCBB.

4. Characterization of CVD diamond for detector applications

We tested exclusively electronic grade plates of oxygen-terminated surface reconstruction. It was shown [23] that nitrogen impurities exceeding 1 ppb are one major defect that controls the electrical properties of scCVDD and that for lower values dislocations seem to play a certain role. The impurity concentrations of 'spectroscopic grade' diamond plates supplied by Ref. [24] are nominally nitrogen, N$<$5 ppb and boron, B$\ll$5 ppb whereas those of pcCVDD films are nitrogen, N$\leq$50 ppb and boron, B$\ll$1 ppb, respectively. The DoI sample presented in this paper is grown using high-purity hydrogen (6.0) without additional nitrogen in the gas mixture. In extended studies with scCVDD films, we probed different surface finishing techniques, in particular polishing by diamond-coated resin wheels and ion-beam polishing. In order to link the electrical characterization results to the crystal quality, atomic force microscopy (AFM) as well as 'white-beam' X-ray topography and birefringence imaging have been performed (Section 4.1).

4.1. Sample preparation and metallization

Prior to the application of contacts in parallel-plate geometry, the diamonds are boiled in oxygen-containing acids, rinsed with ultra-pure water and treated afterwards additionally with oxygen-plasma. A variety of metals and metallic multi-layers have been evaporated or sputtered in order to define the best detector electrodes. We tested the classical variants of annealed Ti–Pt–Au and Cr–Au contacts, and also pure Al or Pd electrodes (not annealed). No convincing influence of the metal choice on the detectors operation or on the characterization data of the CVDD materials has been observed so far. It should be noticed that, for the single-particle readout mode used for hadron sensors, electrodes that reduce the dark conductivity at operation bias
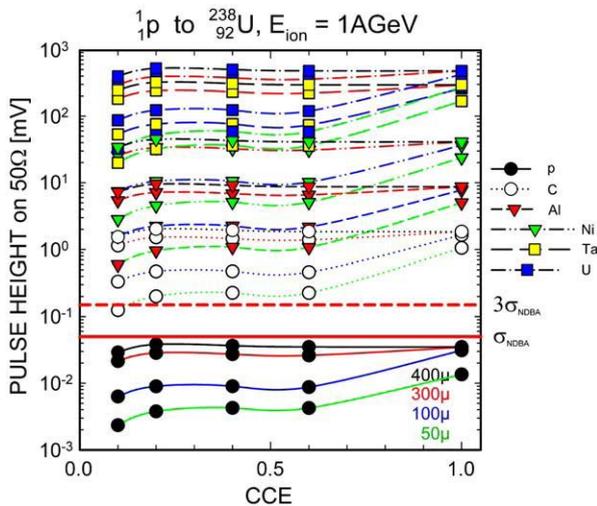
Fig. 2. Estimated amplitudes on 50 Ω input impedance of a DBA amplifier expected from relativistic ions of kinetic energy $E = 1$ AGeV in CVDD sensors of different quality and thickness. The equivalent noise amplitude (rms) of the DBA amplifier is indicated by the solid line at σ_{NDBA} and the noise deviations by the dashed line at $3\sigma_{NDBA}$. The plot demonstrates impressively the large dynamic range of signals involved in hadron physics experiments.

Table 1
Intrinsic time resolution of CVDD sensors.

Test	p, 1.25 GeV	p, 3.5 GeV	p, 6 MeV	^{12}C, 0.4–0.8AMeV	^{27}Al, 2AGeV	^{58}Ni, 1.9AGeV	^{181}Ta, 1AGeV
FEE	CSPA + FEE−1	LCBB	DBA	CSPA + FEE−1	FEE−1	PADI−1	FEE−1
CVDD	SC	SC	SC	SC	SC, PC	PC	PC
σ_i [ps]	330	100	35	60	28, 28	31	25
eff. %	96	94	95	96	92	no data	94

Table 2
Properties of the samples discussed in this article.

Sample	$d_D/\mu m$	Surface finishing	N, B [ppb]	Electrodes; d[nm]	Annealing	Area/mm^2	C_D/pF
pcPF350	350	As grown	≤50; ≪1	Cr/Au;100/200	Ar, 500 °C	Single dot, 50.3	7.3
sc6A	100	Resin-wheel	< 5; ≪5	Al; 100	No	4×q$_x$, 1.5	4×0.8
sc8BP	100	Ion-beam	< 5; ≪5	Al; 100	No	4×q$_x$, 1.5	4×0.8
sc12B	50	Resin-wheel	< 5; ≪5	Al; 100	No	4×q$_x$, 1.5	1.5
DoI549	230	Scaife	Nominally without N	Ti/Pt/Au; 40/50/100	Ar, 500 °C	Single dot, 6.1	1.3

are preferable. On the other hand, charge blocking and release in and from a Schottky barrier may be the reason of an occasionally observed hard breakdown at high rates of ions stopped in the vicinity of the contacts [25].

The growth of evaporated chromium and aluminum on smooth diamond surfaces has been investigated in more detail under high-vacuum conditions by in-situ infrared spectroscopy [26]. A remarkable structural phase transition from a discontinuous phase to the crystalline bulk phase has been observed in ultra-thin Cr at a critical film thickness of $d_{crit} = 2.5$ nm [27]. This value and the IR spectral properties corroborate the old theoretical finding of preferred fcc nanocluster formation of Cr for $d < d_{crit}$ [28], which is an interpretation also supported by the better lattice match of diamond and fcc Cr. Photo-emission-spectroscopy with synchrotron radiation is planned to study the behavior of diamond-carbide-systems [29]. It is known from measurements using silicon-silicide-structures that the height of the barrier does not depend on the metals band structure. It has been suggested that chemical bonds of the interface surface are important [30].

4.2. CVD-diamond surface and bulk structure

The characteristics of the diamond samples exemplarily selected for discussion are listed in Table 2.

For traversing particles, polished surfaces are only required for micro-patterned electrodes. In all other cases, 'as grown' samples are preferable since the surfaces are rough but not damaged. As grown pcCVDD shows a roughness of approximately 10% of the film thickness. AFM pictures illustrating typical defects of differently polished surfaces are shown in Fig. 3(A). The left hand side image demonstrates the atomically flat surfaces of ~0.5 nm (rms) achieved on both sides of the ion-beam polished (IBP) sample sc8BP. Abrasively treated samples show rather different morphology and roughness of opposite sides: sample SC-6A reveals ~6 nm and ~1 nm for side 1 (S1) and side 2 (S2), respectively. In the DoI case, an rms roughness of ~0.9 nm and 2.4 nm, and a maximum depth of scratches of ~7 nm and ~1 nm, respectively, have been achieved by scaife polishing.

Fig. 3B shows 'white-beam' X-ray topographs of the scCVDD samples sc8BP (a) and sc6A (b), respectively. Defect-free regions appear as homogeneous bright areas and dislocations or strain as dark figures. The image of the RWP plate reveals more stress and a higher density of structural defects. The dark regions surrounding a bright spot at the bottom border of the indicated sc6A electrode, point to bundles of threading dislocations found to originate from defects of the HPHT diamond substrate used for growth [25,26,31].

Since threading dislocations may be crucial for the detector operation, birefringence imaging is systematically performed prior to the sensor preparation. Fig. 3C shows full-size pictures of the scCVDD and the DoI sample (a, b, and d), and a part of the larger pcCVDD plate (c), respectively. Structural defects or strain appear in cross-polarized light microscopy bright within homogeneous dark areas of optically isotropic diamond. The sector electrodes applied for electrical characterization are drawn on top of the images.

Little stress but one threading dislocation in each of the scCVDD sample are indicated (sectors q4 of sc8BP and q3 of sc6A). The polycrystalline diamond of 350 μm thickness (c) is produced by polishing a thicker plate on both sides, reducing somewhat the density of dislocations compared to an 'as grown' film. However, the picture illustrates the pcCVDD structure consisting of single-crystal grains separated by grain boundaries. The initial thickness of the DoI film was 300 μm, and the final thickness of 230 μm was achieved by removing 30 μm diamond from the substrate side and some polishing of the uneven growth side. The corresponding image (d) is a consequence of the homogeneous and high nucleation density of diamond on iridium [8], which is still dominant after 30 μm film growth. It would be interesting to investigate whether the removal of more layers from the nucleation side is a way to take advantage of the better lattice match between diamond and iridium.

4.3. Dark conductivity

The IE characteristics of the diamonds are measured in a metallically shielded dark nitrogen atmosphere using Keithley 6517A electrometers. This setup suppresses electrical pick-up, photo excitation and surface humidity. Since an early test has confirmed the measured leakage currents originating from the diamond bulk we do not apply systematically guard ring electrodes. Fig. 4 shows typical IE characteristics of some scCVDD samples (a), diverse 'as grown' pcCVDD films (b), and of the DoI549 plate (c).

Compared to pcCVDD samples (central plot), the dark conductivity of scCVDD is two orders of magnitude lower (left hand plot). However, the behavior of the leakage current versus E_D is similar. It has been shown [32] that the dark conductivity of pcCVDD is governed by transport in the grain boundaries, characterized as thermally activated hopping in antibonding π* and s* states [33]. Recent work on spectroscopic grade diamond revealed that isolated bundles of threading dislocations are dominating the breakdown behavior of single crystals [25]. Homogeneous low conductivity (dark currents<0.1 pA) was measured in all sectors of sample sc8BP up to
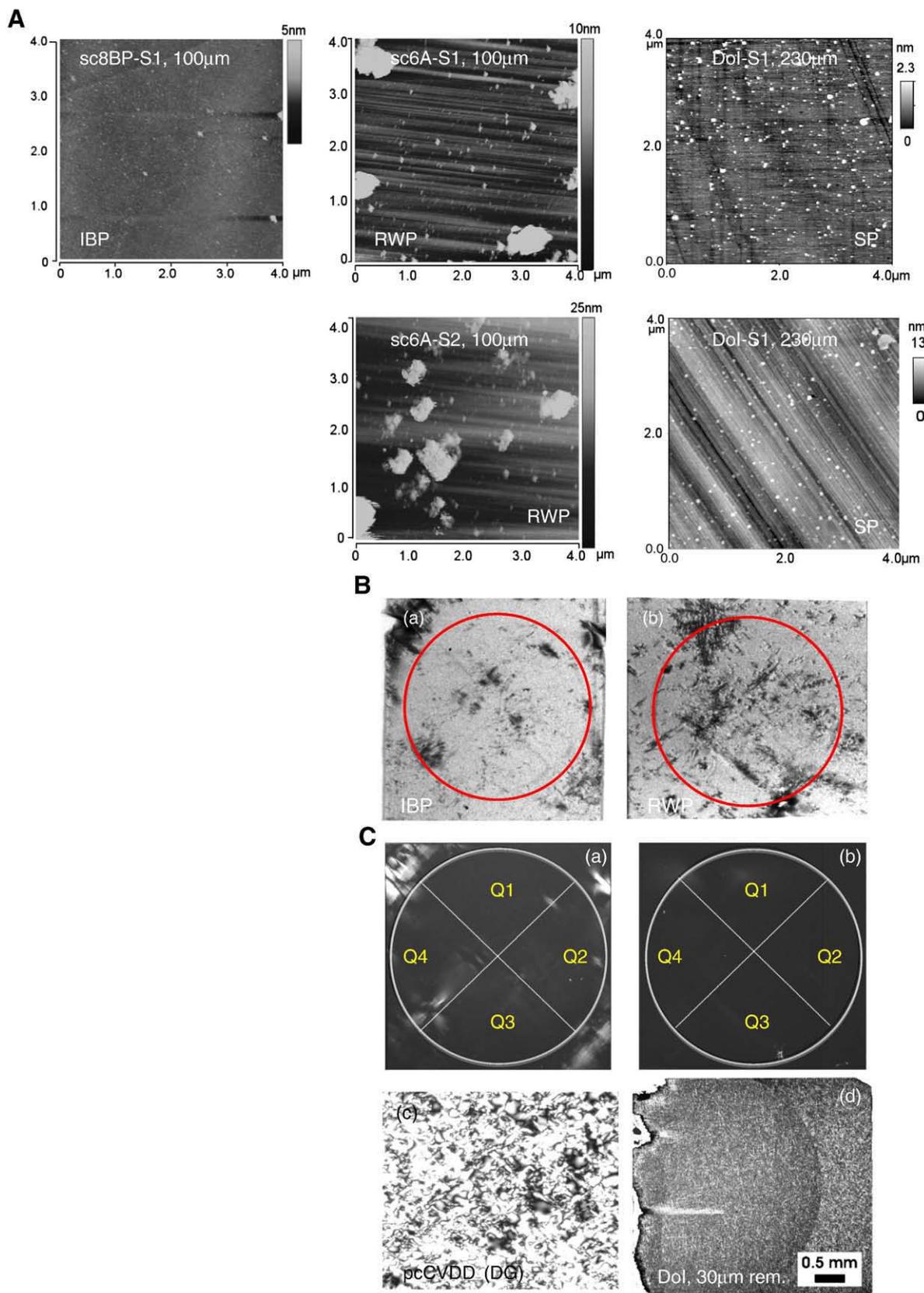
Fig. 3. a. AFM images of the ion-beam polished (IBP) plate sc8B (left picture), the resin-wheel polished (RWP) film sc6A (S1, S 2 central pictures), and the scaife polished (SP) DoI sample (S1, S2 right pictures), respectively. Whereas IBP plates show atomically smooth surfaces on opposite sides, abrasive treatments lead to quite different morphology and roughness which may influence the properties of the contact-diamond interface. b. 'White-beam' X-ray topographs of sc8BP (a) and sc6A (b), respectively. Defect-free regions are indicated by bright areas, whereas dislocations and crystal stress by dark figures. The circles indicate the shape of the electrodes applied afterwards for electrical characterization. The defect density of the RWP sample sc6A is higher. c. Birefringence images of the samples sc8BP (a), sc6A (b), pcPF350 (c), and DoI549 (d). Structural defects and strain appear bright within homogeneous dark areas of optically isotropic diamond. Little stress and isolated dislocations are visible in both homoepitaxial samples, whereas a high defect density is obvious in both heteroepitaxial plates.
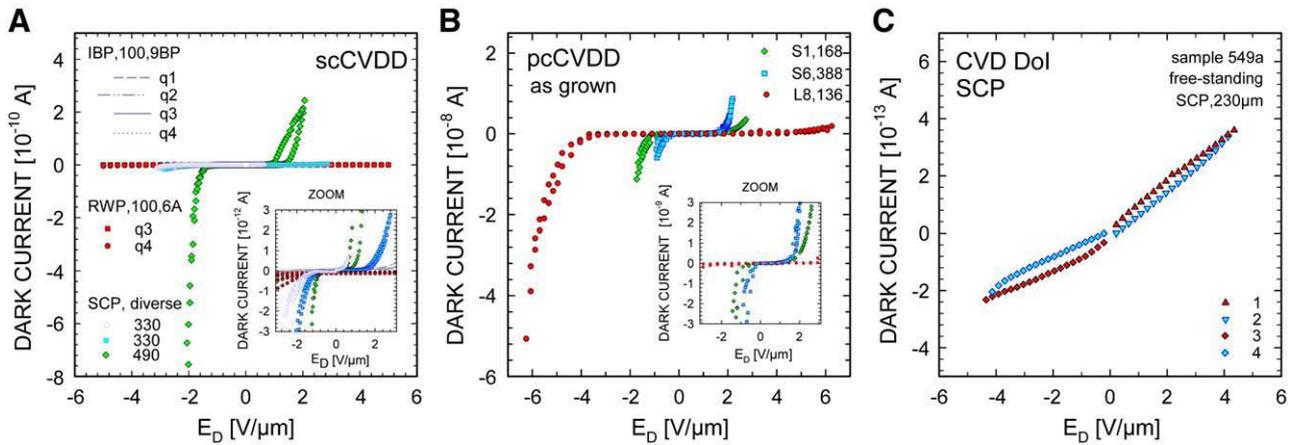
Fig. 4. Typical IE characteristics of scCVDD (A), pcCVDD (B) and DoI (C) samples. Besides the current levels, which deviate by two orders of magnitude, the electric field dependence of the dark conductivity of scCVDD and pcCVDD is similar. (C) The extremely high resistivity obtained from the DoI sample is an experimental result, which needs further detailed investigations (see text).

$E_D = \pm 3$ V/μm (Fig. 5, left). The erratic dark current expected [34] from the threading dislocation in q4 (Fig. 3C(a)) was not observed, or, the image is misleading. Another suggestion is that it appears in conjunction with defective surfaces, which is the case of the mechanically treated film sc6A. In contrast to sc8BP, a strong increase of the dark current has been measured in sector q_3 of sample sc6A (Fig. 5, right) at relatively low-field $E_D \sim \pm 1.2$ V/μm. In addition, polarization (q_4) and memory effects (q_3 and q_4) appear. The different behavior of the currents obtained from q_1 and q_4 (revealing similar extended defects), may indicate either coplanar roughness inhomogeneities, or a dependence of the dark conductivity on the inclination angle between dislocations and the (100) E-field direction.

The measured IE curves are in good agreement with the space charge limited conductivity mechanism (SCLC) [25,35]. Two distinct ranges are measured for pcCVDD and scCVDD samples: the 'safe detector bias range', where the measured dark current shows an Ohmic or blocking behavior on the sensitivity limit of the measurement system, and the 'soft breakdown' regime, where the curves are described by a single power law $I \sim E^\alpha$ with an exponent $\alpha = 2.2$ for 'defect-free' films and 5–7 for lower quality samples [25]. In addition, blue-light electroluminescence was observed from defective scCVDD plates (Fig. 6, left), which was correlated with extended structural defects, as it is confirmed from the corresponding X-ray topograph (Fig. 6, central). The Gaussian peaking at 2.84 eV ($\sigma = 0.16$ eV) which is shown on the right graph of the figure is the spectrum of the light emitted. The power-low exponents of $\alpha \gg 2$ in conjunction with the broad width of the emitted light distributions indicate that charge recombined rather at a band than at discrete levels. It is suggested that

such a band in the forbidden gap is formed by dislocations or other extended structural defects (for instance stress or bundles of dislocations). Defect-free samples does not show light emission, even at much higher electric fields [25].

Up to present, the attempt to understand the dark conductivity of DoI diamond the same way as of the other CVDD types failed. Based on the applied growth conditions (Table 2) we assumed diamond of rather high purity. However, the N and B concentrations are not measured so far. The very low dark current obtained is in contradiction to the birefringence image. Following the idea that charge transport in dislocations controls the dark conductivity of CVDD, a much higher dark current was expected. An assumption that the dislocations of DoI samples do not release charge is unlikely. Conceivable is that the dark current vanishes due to the compensation of shallow traps by deep defect levels (compare Section 4.6). In that case, a significant loss of the particle induced charge and a very short charge-transition time are expected. The positive aspect is the predicted high breakdown field of DoI sensors (Fig. 4C).

4.4. Transient current signals

The TC technique (TCT) is based on the fact that the transition time $t_{tr}^{e,h}$ of the ion-generated charge from the point of pair separation to the electrode is given by the width of the TC signals. The short range of ^{241}Am-α-particles in diamond $R_{Dia}^\alpha = (12 \pm 5)\mu m$ renders possible to control the drift of electrons and holes by the bias polarity of the electrode impinged by the particles; the longer drift distance corresponds (almost) to the detector thickness being $d_D \gg R$ and the
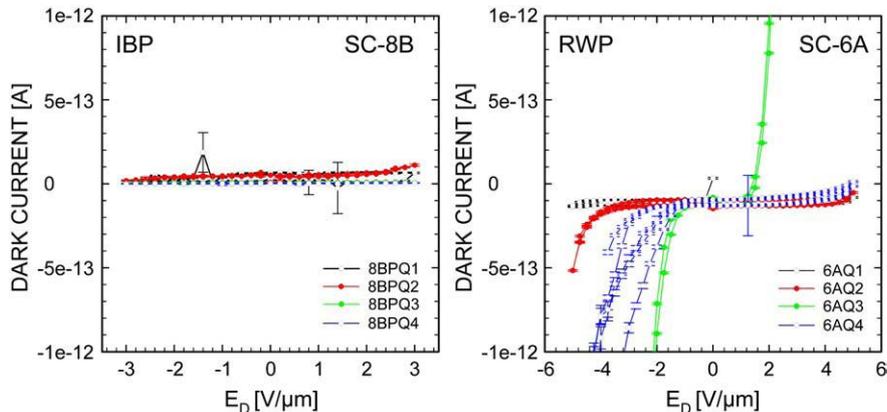
Fig. 5. Dark current behavior in sectors Q1–Q4 of the ion-beam polished sample sc8BP (left) and the resin-wheel treated sample sc6A (right), respectively. The erratic current expected from threading dislocations is observed only in conjunction with the defective surfaces of the resin-wheel polished sample sc6A.
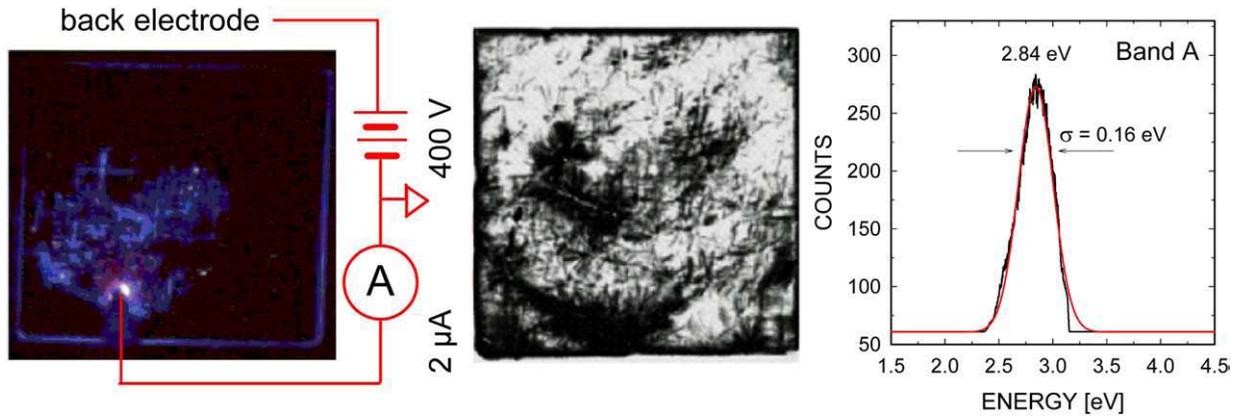
Fig. 6. (left) Electroluminescence observed from extended structural defects of a scCVDD sample in 'hard breakdown'. The X-ray topograph of the film shown in the central picture confirms the origin of the blue-light emission. The broad Gaussian distribution of the emitted light peaking at 2.84 eV indicates charge recombination at a band formed in the forbidden gap by extended structural defects or strain.

drift velocities are given by $v_{drift} = d_D/FWHM$. The signal shape illustrates the internal electric field profile for the single-carrier drift in the small-signal case, as well as possible trap and space charge concentrations in the sensors [36,37].

However, TCT applies precisely only for crystal detectors in which the majority of the charge carriers reach the sensor electrodes. Fig. 7 shows the development of α-induced current pulses at increasing E_D in diamonds of different quality and thickness: a defect-free scCVDD sensor of 400 μm thickness (Fig. 7A), as well as the pcPF350 (Fig. 7C) and the DoI549 (Fig. 7D) sensors, respectively. In all measurements, the DBA amplifier was reading out the signals through the biasing electrode irradiated by the α-source installed at growth side; hole-

drift signals are the positive pulses. The pcCVDD and the DoI sensors have been tested in the primed state [19]. 'High-frequency ringing' of the scCVDD signals is caused by some unavoidable impedance mismatching.

As expected, the first conspicuous distinction is the extremely different transition time of the charge carriers, which eventually defines the single-particle rate capability of the different CVDD types. In the case of the scCVDD pulses, the slopeless flattop of the signals demonstrates negligible space charge and comparable drift velocity of electrons and holes [18] moving in a constant field $E_D(100)$ (Fig. 7A). Indeed, the measured drift velocities at a safe detector operation bias amounted to $v_h \sim 110 \, \mu m/ns$ for holes and $v_e \sim 90 \, \mu m/ns$ for electrons, whereas the
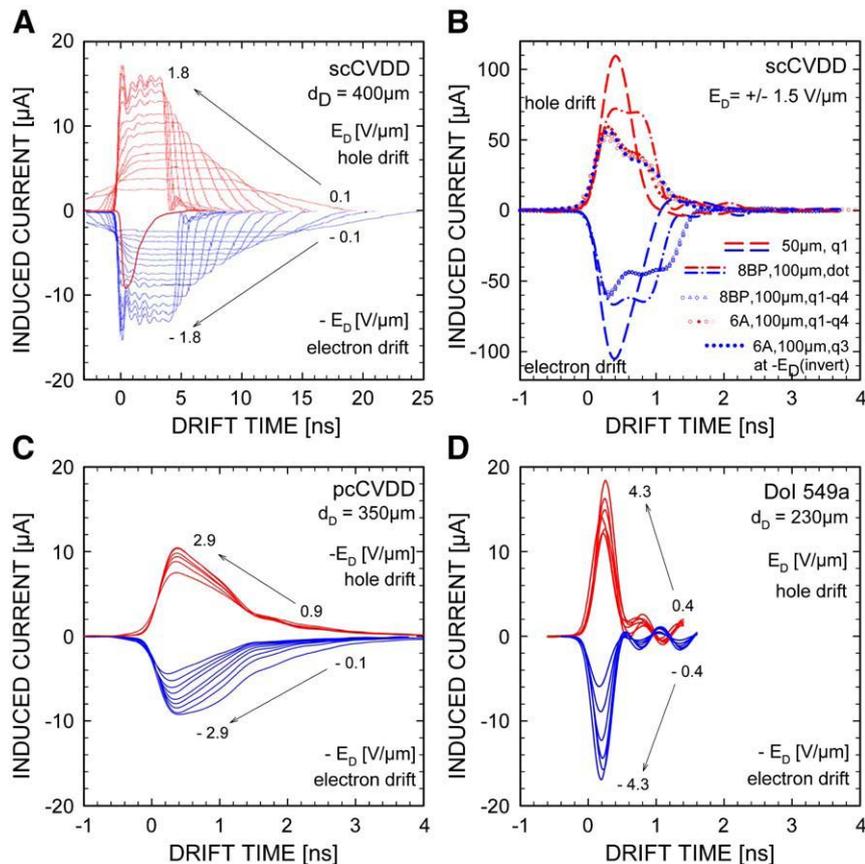
Fig. 7. Development of ^{241}Am-α-pulses at increasing electric field in diamond sensors of different quality and thickness. Hole-drift signals are displayed positively and electron-drift pulses negatively. (A) scCVDD of $d_D = 400$ μm; (B) scCVDD: dashed line: $d_D = 50$ μm (q1), dash–dot line: $d_{8BP} = 100$ μm (3 mm dot electrode), incrementing symbols: d_{8BP} and d_{6A} (q1–q4), dotted line: inverted electron signal 6Aq4; (C) pcPF350; (D) DoI549. The signals in (C) and (D) are measured in the 'pumped state'.

extrapolated low-field mobilities and saturation velocities obtained by fitting the experimental data achieve values (μ_{0-e} = 1300–3100 cm²/Vs; v_{e-sat} = 190 µm/ns) and (μ_{0-h} = 2400 cm²/Vs; v_{h-sat} = 140 µm/ns) for electrons and holes, respectively [38]. These results are in good agreement with other measurements using the same technique at comparable high bias values as required for particle detector operation [39]. Note that complete velocity saturation has not been observed despite the very high bias applied. In Fig. 7(B) are signals compared, which have been recorded from scCVDD of a thickness of 50 µm (dashed lines) and of 100 µm (dashed–dot lines), respectively. The linear dependence of the signals FWHM on $1/d_D$ is obvious in this case of complete charge-collection. The groups of signals (incrementing symbols) have been obtained from the sectors q1–q4 of samples sc8BP (electrons) and sc6A (holes), respectively, demonstrating spatial homogeneity of the detector response. The inverted electron pulse has been overlaid on the corresponding 6Aq4 hole signal (dotted line) in order to test polarization. The different behavior of the dark current by inverting the bias (see Fig. 5) does not affect significantly the electric field profile.

In contrast to 'as grown' samples, which show rapid charge quenching indicated by inhomogeneous triangular signal shapes [40], this 'detector grade' pcPF350 show two distinguished regions for both electrons and holes drift. The signals develop an obvious 'cusp', which shifts with increasing bias. This may indicate a decrease of the effective sample thickness [18], for instance by accumulation of electrons beneath the anode due to charge injection. At present, only such speculations can be expressed concerning the unexpected long signal tails obtained. Either this observation is due to charge injection, or there are crystal regions of significantly longer charge-carrier lifetimes. However, the slopes of the 'flattops' demonstrate clearly a significant charge trapping but no space charge.

The extremely narrow width of the DoI pulses confirms the suggestion (Section 4.3) that the high amount of dislocations in this type of diamond leads to massive loss of the particle induced charge. The positive message from this first result is that a detector material of highest single-particle rate capability can be envisaged, suitable for heavy-ion-beam monitoring and ion-ToF in experiments with high-intensity ion-beams. Despite the significant charge trapping, the induced current amplitudes obtained (Fig. 7D) have been on the order of the pulse heights of thick spectroscopic grade samples (Fig. 7A). The rate capabilities of pcCVDD and scCVDD sensors are confirmed to about 5×10^8 [17] and $>10^7$ Hz [25], respectively.

4.5. Charge-collection efficiency

In order to operate diamond sensors as single-particle ionization chambers for ion spectroscopy, the collected charge Q_C has to be equal to the primary ionization charge Q_G generated from each ion. For this, a $CCE(E) = Q_C(E)/Q_G$ close to unity is required. Note that for simple counting or ion-ToF measurements of highly ionizing ions, a CCE < 1 is acceptable as far as the detection efficiency, (i.e. the ratio of the detected particles to the impinging ions) is on the order of ~ 100%.

The generated number of electron-hole pairs (e–h) in a diamond sensor is given by $N_G = \Delta E / \varepsilon_{Dia}^{pp}$, where ΔE is the ionizing energy-loss of the particle and ε_{Dia}^{pp} ~ 13 eV/e–h the pair-production energy in diamond. The relatively high value of ε_{Dia}^{pp} (compare silicon with 3.6 eV/e–h), is a serious disadvantage in detector applications leading to small S/N ratios. The dependence of the CCE(E) of crystal detectors on impurities and dislocations is described by Hecht's formalism [41] given by Eq. (3). Karl Hecht introduces the 'Schubweg', $w_x(E)$, as the average drift distance in the direction of the external E-field, within which the amount of collected electrons has decreased to the 1/e value of the generated charge carriers. The $1/w_x(E)$ value is thereby understood as the E-field dependent absorption constant of defective crystals.

$$CCE(E) = \frac{Q_C(E)}{Q_G} = \frac{w_x(E)}{d_D} \cdot \left(1 - e^{-\frac{x}{w_x(E)}} \right) \tag{3}$$

with $Q_C(E) = q_e \cdot N_C(E)$, $Q_G = q_e \cdot N_G$ the collected and the generated charge, respectively, q_e the electron charge, d_D the detector thickness, and $w_x(E)$ the 'Schubweg'.

The evidence of this exponential is crucial for the design of diamond sensors. The message is that a CCE equal to unity is impossible; furthermore that for $w_x(E)$ equal to the detector thickness, the collected charge amounts only to 63.2% of the generated charge, whereas a $w_x(E) \gg 100 \cdot d_D$ is required for the collection of about 99% of Q_G.

Fig. 8 (left) illustrates the general trend of the CCE(E) characteristics of scCVDD and pcCVDD as well as of 'early' DoI material: the three tested diamond types are represented by sample sc12B (diamonds), pcPF350 (circles), and DoI549 (triangles), respectively. Note that the 'error bars' indicate the widths of the measured $Q_C(E)$ distributions (Fig. 8, right graph), whereas the uncertainties of the CCE mean values are small.

The characterization of the CCE and of the energy resolution $\delta E/E$ is usually performed under vacuum conditions using CS detector readout. Since these measurements have not been performed so far with the DoI sensor, we present systematic data measured in air with DBA amplifiers; the data are corrected by taken into account the energy-loss of the α-particles in the 5 mm air distance between source and diamond surface (i.e., ΔE_α = 0.54 MeV or ΔQ_G^α = 6.7 fC).
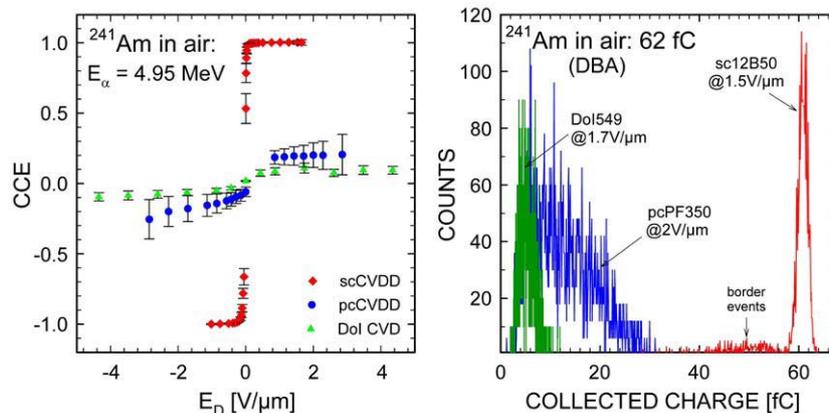
Fig. 8. (left) The behavior of the charge-collection efficiency (CCE) of the three CVDD types, as measured with a DBA while the α-source was mounted in air at distance of 5 mm from the sensors growth side. The 'error bars' represent the σ-widths of the collected charge distributions shown on the right graph of the figure. (right) Collected charge spectra obtained from all sensors at a similar electric field E_D~ 2 V/µm.

Almost full saturation of the collected charge to a CCE ~ 0.95 is obtained for sc12B at very low fields $E_D \leq 0.2$ V/µm for holes drift and slightly higher E_D for electrons drift. The CCE of the pcPF350 sensor amounts to 0.2 for holes and to 0.25 for electrons, respectively. The successive increase of the mean value and the width by increasing the bias demonstrates improving charge-collection but also a deteriorating energy resolution of the sensors. This trend is also confirmed by the TCT results shown in Fig. 7. The DoI sample shows a rather symmetric characteristic with slightly better efficiency for holes drift (CCE ~ 0.12), and significantly less spread of the collected charge distributions compared to pcCVDD (Fig. 8, right graph). These results are in agreement with heavy-ion data published in [42].

As expected for fully depleted high-quality sensors, the energy resolution of scCVDD detectors improves with increasing bias. Therefore, also devices implemented for ion spectroscopy profit from a high breakdown field and a fast collection of charge [14]. Note that a reasonably good $\delta E/E$ is always required for background reductions, even in experiments in which the sensor task is solely the timing. To our opinion, scCVDD is the only known detector material combining energy and time resolution in such an excellent manner. For ^{241}Am-α's and light ions, spectroscopic grade diamond shows a $\delta E/E \sim 0.003$, which is comparable to the resolution of silicon sensors measured under same conditions [43], and a $\delta E/E \sim 0.02$ for ions of $A > 40$ which is superior to the silicon ones. As discussed in [14], in contrast to the high-mobility diamond sensors, silicon detectors deteriorate at SCLC transport showing pulse-height defects (plasma effect).

4.6. A radiation hardness study of scCVDD diamond plates

The detector characteristics of scCVDD samples measured in the virgin state was compared to the properties obtained after heavy irradiations with 26 MeV protons and 20 MeV neutrons [6,25], as well as with electrons of 10 MeV [12]. The integral particle fluencies were $\Phi \geq 10^{16}$ (p,n)/cm^2 for the hadron-irradiated films, whereas in the electron case a fluence of an equivalent dose of 10 MGy was applied. For details see Refs. [6,25] and [12], respectively. The conclusion of all data is that a stable operation of the sensors with MIP distributions separated from the electronic noise is confirmed within the hadron-fluence range tested, whereas the sensors have been still operational after absorbing relativistic electrons of a dose equivalent of ~7MGy.

However, radiation-induced defects of the detector signals were observed in all cases. In the following we will discuss in more detail the defects induced by protons and neutrons. Note that the described study has been performed with thick diamond sensors ($d_D \sim 400$–500 µm) while expecting that thinner samples ($d_D \sim 50$–100 µm) show better radiation resistance [25]. OAS in the UV–VIS range shows [25] that the main surviving defects are neutral mono-vacancies V^0, identified in all measured spectra by a characteristic zero-phonon line at 1.638 eV. TCT has been applied to measure effective deep-trapping lifetimes $\tau_{e,h}$, and a linear scaling of $1/\tau_{e,h}$ with fluence has been obtained as well as almost identical defect production rates for both neutron and proton irradiations. The neutral state of the defects was confirmed by the absence of space charge and no degradation of the carriers drift velocity, both visible in the TC signals. Due to migration and recombination of the neutral mono-vacancies, a permanent recovery of the CCE was achieved after high-temperature annealing (>800 °C). It was also possible to prime sensors irradiated by up to F ~ 10^{14} particles/cm^2 with ^{90}Sr electrons to almost the initial CCE value.

In contrast to damaged silicon sensors, the dark conductivity of irradiated diamond detectors is decreased. The same observation was found for irradiated pcCVDD devices [1]. In the scCVDD case, this is most likely due to a compensation of shallow traps by neutral vacancies. However, these results confirm the assumption that, in order to understand the dark conductivity of CVDD, more parameters than nitrogen concentrations and crystal dislocations (found to control the

dark current in high-purity virgin samples) have to be considered. In addition, the behavior of the simultaneously irradiated detector electrodes and the possible consequences for the diamond-contact interface has to be systematically investigated.

5. Summary and conclusions

In this article, we have discussed the potential of electronic grade CVDD materials for detector applications in hadron physics research. The characteristics of diamond sensors consisting of scCVDD and pcCVDD plates have been compared to recent results obtained from 'early' DoI sensors grown on the multi-layer substrate Ir/YSZ/Si001. In addition, the important role of the front-end electronics has been addressed in conjunction to the large dynamic range of signals to be processed in hadron physics experiments. It was shown that the best diamond quality is not necessarily the best choice for heavy-ion beam monitoring or timing measurements but an indispensable requirement for ion spectroscopy and for time measurements of relativistic ions lighter than carbon.

The central material properties justifying diamond detectors as being superior to comparable classical sensors are the high breakdown fields observed in conjunction with the high drift velocities of both charge carriers. It is evident that these characteristics support high rate single-particle counting and ion-ToF applications. In addition, they are the reason for the excellent energy resolution of diamond sensors applied for spectroscopy of highly ionizing ions where the detectors operate in the SCLC regime. The preliminary radiation hardness study with protons and neutrons revealed a linear decrease of the collected charge to about 15% of the initial value which corresponds to a MIP signal still separated from the electronic noise of the spectroscopy amplifiers. Similar values have been measured recently for silicon sensors. The advantages of heavily irradiated diamond detectors with respect to this issue are: the decreasing dark conductivity and the still excellent timing properties, most likely sustained due to the predominant creation of neutral vacancies (V^0).

The comparison of the heteroepitaxially grown diamond sensors revealed a lower CCE for the tested DoI sensor, which is in accordance to the higher dislocation density observed in birefringence images. Nevertheless, the high breakdown stability and the strong induced current amplitudes obtained in conjunction with a homogeneous distribution of the structural defects are favourable. We expect a similar heavy-ion time resolution as of the pcCVDD sensors as well as improved position and energy resolutions. In addition that further material removal from the nucleation side will lead to significantly improved charge-collection properties.

Summarizing the results of all tested diamond materials, we conclude that the combination of radiation resistance, high rate capability, and time resolution leads to extraordinary heavy-ion timing detectors superior to plastic scintillation counters, proportional chambers, or channel plates used usually for these purposes. High-quality scCVDD sensors are competitive to silicon detectors in heavy-ion spectroscopy and in any position sensitive measurement that requires charge-sharing between strips. On the other hand, the higher material budget required and the deteriorated charge-collection properties after heavy irradiation thwart at present the emergence of a serious competition to silicon devices in MIP tracking applications. Despite all hesitations, the most of the scientific groups collaborating at FAIR have included pcCVDD as well as scCVDD sensors in their Technical Proposals for the Design, Construction, Commissioning and Operation of FAIR experiments [44].

References

[1] H. Kagan, W. Trishuk, in: R.S. Sussmann (Ed.), CVD Diamond for Electronic Devices and Sensors, Wiley Series Materials for Electronic & Optoelectronic Applications, 2009, p. 207.
[2] E. Berdermann, K. Blasche, P. Moritz, H. Stelzer, B. Voss, F. Zeytouni, Nucl. Phys. B 78 (1999) 533.
[3] A. Oh, PhD thesis, Universität Hamburg (1999).
[4] G. Verona-Rinati, in: R.S. Sussmann (Ed.), CVD Diamond for Electronic Devices and Sensors, Wiley Series Materials for Electronic & Optoelectronic Applications, 2009, p. 257.
[5] J. Morse, M. Salomè, E. Berdermann, M. Pomorski, W. Cunningham, J. Grant, Diamond Relat. Mater. 16 (2007) 1049.
[6] Wim de Boer, J. Bol, A. Furgeri, S. Mueller, C. Sander, E. Berdermann, M. Pomorski, M. Huhtinen, Phys. Status Solidi (A) 204 (9) (2007) 3004.
[7] G. Kramberger, for the RD50 Collaboration, NIMA 583 (2007) 49.
[8] M. Schreck, in: R.S. Sussmann (Ed.), CVD Diamond for Electronic Devices and Sensors, Wiley Series Materials for Electronic & Optoelectronic Applications, 2009, p. 125.
[9] P. Braun-Munzinger, Johanna Stachel, Nature 7151 (2007) 302.
[10] P. Moritz, E. Berdermann, K. Blasche, H. Stelzer, F. Zeytouni, Proc. AIP Conference, Stanford CA, 1998.
[11] S. Mueller, W. de Boer, M. Schneider, A. Saballek, M. Schmanau, C. Ruehle, T. Schneider, and R. Hall-Wilton, Phys. Status Solidi (A) 206 (9) (2009) 2091.
[12] C. Grah, K. Afanaciev, I. Emeliantchik, U. Harder, H. Henschel, A. Ignatenko, E. Kouznetsova, W. Lange, W. Lohmann, M. Ohlerich, Ringo Schmidt, IEEE Trans. Nucl. Sci. 56 (2) (2009) (April).
[13] J. Lindhard, A.H. Sørensen, Phys. Rev. A 53 (1996) 2443.
[14] E. Berdermann, A. Caragheorgheopol, M. Ciobanu, M. Pomorski, A. Pullia, S. Riboldi, M. Traeger, H. Weick, Diamond Relat. Mater. 17 (2008) 1159.
[15] The NUSTAR SuperFRS and R3B Collaborations, Technical Design Proposal, 2005.
[16] E. Berdermann, M. Ciobanu, in: R.S. Sussmann (Ed.), CVD Diamond for Electronic Devices and Sensors, Wiley Series Materials for Electronic & Optoelectronic Applications, 2009, p. 227.
[17] P. Moritz, E. Berdermann, K. Blasche, H. Stelzer, B. Voss, Diamond Relat. Mater. 10 (2001).
[18] G. Juška, M. Viliunas, O. Klíma, E. Šípek, J. Kočka, Philos. Mag. B 69 (1994) 277.
[19] [19] D. Meier, PhD Thesis, Ruprecht-Karls Universität Heidelberg, (1999).
[20] [20] H. Spieler, Fast timing methods for semiconductor detectors, IEEE Transactions on Nuclear 36 Science, 29, 1142-1158 (1982).
[21] M. Ciobanu, A. Schüttauf, E. Cordier, N. Herrmann, K.D. Hildenbrand, Y.J. Kim, Y. Leifels, M. Marquardt, M. Kiš, P. Koczon, X. Lopez, M. Petrovici, J. Weinert, X.J. Zhang, IEEE TNS 54 (2007) 1201.
[22] W. Koenig, J. Pietraszko, for the HADES Collaboration, GSI Ann. Rep. (2008).
[23] A. Secroun, O. Brinza, A. Tardieu, J. Achard, F. Silva, X. Bonnin, K. De Corte, A. Anthonis, M.E. Newton, J. Ristein, P. Geithner, A. Gicquel, Phys. Status Solidi (A) 204 (12) (2007) 4298.
[24] Diamond Detectors Ltd., Poole, Dorset, UK.
[25] M. Pomorski, PhD thesis (2008), Goethe Universität Frankfurt.
[26] R. Lovrinčić, PhD thesis (2009), Ruprecht-Karls Universität Heidelberg.
[27] R. Lovrinčić and A. Pucci, Infrared optical properties of chromium nanoscale films with a phase transition, Phys. Rev. B 80 (2009) 205404.
[28] S.H. Huh, H.K. Kim, J.W. Park, G.H. Lee, Phys. Rev. B 62 (2000) 2937.
[29] D. Semmler, Internal Proposal.
[30] R.J. Purtell, P.S. Ho, G.W. Rubloff, P.E. Schmidt, Physica 117&118B (1983) 834.
[31] M.P. Gaukroger, P.M. Martineau, M.J. Crowder, I. Friel, S.D. Williams, D.J. Twitchen, Diamond Relat. Mater. 17 (2008) 262.
[32] C.E. Nebel, A. Waltenspiel, M. Stutzmann, M. Paul, L. Schäfer, Diamond Relat. Mater. 9 (2000) 404.
[33] B.I. Sklovskii, E.I. Levin, H. Fritsche, S.D. Baranovskii, in: H. Fritsche (Ed.), Advances in Disordered Semiconductors, vol. 3, World Scientific, Singapore, 1990, p. 161.
[34] J. Yang, W. Huang, T.P. Chow, J.E. Butler, Proc. MRS, 2005, 0905-DD06-09.
[35] S. Nespurek, P. Smejtek, Czech. J. Phys. B 22 (1972) 160.
[36] J. Isberg, Phys. Status Solidi (A) 202 (11) (2005) 2194.
[37] M. Nesladek, Anna Bogdan, W. Deferme, N. Tranchant, P. Bergonzo, Diamond Relat. Mater. 17 (2008) 1235.
[38] M. Pomorski, E. Berdermann, A. Caragheorgheopol, M. Ciobanu, M. Kiš, A. Martemiyanov, C. Nebel, P. Moritz, Phys. Status Solidi (A) 203 (12) (2006) 3152.
[39] H. Pernegger, Phys. Status Solidi (A) 203 (13) (2006) 3299.
[40] E. Berdermann, K. Blasche, P. Moritz, H. Stelzer, B. Voss, F. Zeytouni, Nucl. Phys. B 78 (1999) 533.
[41] K. Hecht, Z. Phys. 77 (1932) 235.
[42] A. Stolz, M. Behravan, M. Regmi, B. Golding, Diamond Relat. Mater. 15 (2006) 807.
[43] E. Berdermann, for the NoRHDia Collaboration, in: I. Iori (Ed.), Proc. XLIII Intern. Winter Meeting on Nuclear Physics, Bormio, Italy, 2005, p. 371.
[44] http://www.gsi.de/fair/experiments/.